Acta Biomaterialia 112 (2020) 213–224

Contents lists available at ScienceDirect

Acta Biomaterialia

journal homepage: www.elsevier.com/locate/actbio

Full length article

Cholla cactus frames as lightweight and torsionally tough biological materials

Luca De Vivo, (CO)[a,*], Albert K. Matsushita, (CO)[b], Daniel Kupor[c], Josue Luna[b], Beatrice A. Tierra[d], Rober L. Sah[d], Vlado A. Lubarda[b,e], Marc A. Meyers[b,e], Joanna M. McKittrick[b], Petr Krysl[a], Falko Kuester[a]

[a] Department of Structural Engineering, University of California, San Diego, 9500 Gilman Dr., La Jolla, CA, 92093, USA
[b] Department of Mechanical and Aerospace Engineering and Materials Science and Engineering Program, University of California, San Diego, 9500 Gilman Dr., La Jolla, CA, 92093, USA
[c] Department of Chemical Engineering, University of California, San Diego, 9500 Gilman Dr., La Jolla, CA, 92093, USA
[d] Department of Bioengineering, University of California, San Diego, 9500 Gilman Dr., La Jolla, CA, 92093, USA
[e] Department of Nanoengineering, University of California, San Diego, 9500 Gilman Dr., La Jolla, CA, 92093, USA

ARTICLE INFO

Article history:
Received 16 December 2019
Revised 24 April 2020
Accepted 30 April 2020
Available online 13 May 2020

Keywords:
Biological materials
Cholla cactus
Finite element analysis
Torsion

ABSTRACT

Biological materials tested in compression, tension, and impact inspire designs for strong and tough materials, but torsion is a relatively neglected loading mode. The wood skeletons of cholla cacti, subject to spartan desert conditions and hurricane force winds, provide a new template for torsionally resilient biological materials. Novel mesostructural characterization methods of laser-scanning and photogrammetry are used alongside traditional optical microscopy, scanning electron microscopy, and micro-computed tomography to identify mechanisms responsible for torsional resistance. These methods, in combination with finite element analysis reveal how cholla meso and macro-porosity and fibril orientation contribute to highly density-efficient mechanical behavior. Selective lignification and macroscopic tubercle pore geometry contribute to density-efficient shear stiffness, while mesoscopic wood fiber straightening, delamination, pore collapse, and fiber pullout provide extrinsic toughening mechanisms. These energy absorbing mechanisms are enabled by the hydrated material level properties. Together, these hierarchical behaviors allow the cholla to far exceed bamboo and trabecular bone in its ability to combine specific torsional stiffness, strength, and toughness.

Statement of Significance

The Cholla cactus experiences, due to the high velocity desert winds, high torsional loads. Our study has revealed the amazingly ingenious strategy by which the tubular structure containing arrays of voids intermeshed with wood fibers resists these high loads. Deformation is governed by compressive and tensile stresses which are greatest at 45 degrees to the cross section. It proceeds by stretching, sliding, and bending of the wood fibers which are coupled with the pore collapse, resulting in delayed failure and a high torsional toughness.

1. Introduction

Researchers have been studying biological materials for their superbly efficient mechanical properties, discovering a variety of hierarchical architectures responsible for them. For example, Bouligand structures found in mantis shrimp dactyl clubs provide

* Corresponding Author.
E-mail addresses: ldevivo@ucsd.edu, ghannams@livemail.uthscsa.edu (L. De Vivo).

https://doi.org/10.1016/j.actbio.2020.04.054

extrinsic toughening (i.e., crack driving suppression as opposed to crack initiation suppression) via crack deflection under impact. The combination of dense and cellular structures found in cortical and trabecular bone respectively provide weight-efficient stiffness and strength [1,2]. Nacre comprises interdigitating ceramic plates in a protein matrix that combine crack deflection, pull-out and frictional resistance, and sacrificial bonds to greatly increase toughness and strength [3–5]. Most of these investigations for sources of bio-inspiration, however, have focused on compressive or tensile modes of loading [6,7]. Studies of how natural materials bear torsional loads may unlock new bio-inspired structural design elements with applications in structural and aerospace industries.

To this end, we may turn to free-standing plants which bear a combination of axial loading, bending, and torsion to support their own mass against gravity, wind, or snowfall. Their adaptations to torsion broadly fit into the categories of minimizing or maximizing torsional stiffness [8]. Petioles (leaf stems) exemplify the former: their cross-sections maximize the bending moment to support leaves for proper exposure to the sun, but minimize the torsional moment to allow twisting under high winds, thereby reducing drag [9]. On the other hand, primary structural materials (i.e. tree stalks and trunks) typically exhibit torsional stiffness. We hereby focus on this latter category of adaptation as it is applicable to structures such as driveshafts.

To understand the torsional behavior of trees, we must understand the wood of which they are made. It is a closed-foam, anisotropic cellular solid with three perpendicular directions defining its orthotropy: the axial (vertical direction of growth), radial (from the plant center to the periphery), and the tangential (perpendicular to both axial and radial directions). Wood anatomy is characterized by three mesostructural features: tracheids, rays, and vessels. Tracheids describe the long, axially growing cells comprising the bulk of trees. Rays are rectangular, radial arrays of cells responsible for the transport of nutrients and fluids from the center of a tree to the periphery, where growth occurs. Finally, vessels are enlarged, thin walled pores that conduct fluids vertically and only found in angiosperms [10]. Wood is weaker in longitudinal shear (shear plane parallel to longitudinal axis) than in transverse shear (shear plane perpendicular to longitudinal axis); pure torsion about the longitudinal axis results in failure along the axial direction (although shear stiffness in the radial-tangential (R-T) plane is the lowest, shear strength is lowest in the axial-radial (A-R) plane).

Evenly exposed to a uniform wind field, a radially symmetric plant would strictly bend—such a condition, however, is exceedingly rare. A non-uniform wind field, radial asymmetry in the canopy or the roots, and shielding by neighboring features of the landscape can all cause a plant to undergo additionally torsion [11]. In modeling the bending and twisting of a tree due to wind, Skatter and Kucera [12] found that isolated spruce trees were as likely to fail in either mode. This finding was supported by the observation that after a storm in Switzerland, 11% of fell spruces failed in bending and 17% in torsion [13]. As the ratio of a tree's height to its skewness (the projected offset of the plant's crown from its roots) decreases, the likelihood of twisting failure linearly increases. Thus, tall and slender trees with a tight crown of low skewness, such as spruce, are as likely to fail in bending as in torsion, while shorter trees with a distributed and highly skewed crown are more likely to fail in torsion.

Trees possess several adaptations to resist these torsional loads. At the macroscopic scale, Norwegian spruce trees (Fig. 1a, i) can grow axially spiraling fibers (called spiral grain) that become visible in trunks or logs split along fibers in the A-R plane (Fig. 1a, ii). The torsional strength is increased in the direction of chirality, and depending on prevailing wind direction, trees of the same species can grow spirals of different handedness and even grow branches asymmetrically to encourage twisting in the stronger direction [11,12,14]. More generally, a tree can grow or shed branches to act as dynamic mass dampers and mitigate harmonic and resonant swaying frequencies, minimizing the transfer of wind bending and torsion to the trunk and root system [15]. Trees also exhibit a gradient of increasing axial stiffness from the center to the periphery, with an order of magnitude difference in Young's modulus. The gradient reflects an optimization for flexibility during the tree's early life, but as the tree matures and grows a larger crown it requires greater stiffness to prevent Euler buckling [16]. The increased stiffness at the tree's periphery also enhances its torsional strength as the stresses increase linearly with distance from the neutral axis [8,17,18].

Bamboo has also been studied in torsion for new potential applications in construction that go beyond its traditional known strengths in axial compression and bending [17,19]. Consisting of a hollow shaft separated by nodes into sections called culms or internodes as illustrated in Fig. 1b, i, bamboo is a natural composite. At the meso-scale it comprises dense vascular bundles of heavily lignified structural cells embedded in a matrix of thin-walled living (parenchyma) cells. From the inner to the outer surface of the culm, the frequency of vascular bundles and their volume fraction increases to produce a positive radial density gradient, which leads to correspondingly increasing gradients of stiffness and strength (Fig. 1b, ii). This arrangement allows the bamboo to optimize the moment of inertia to resist bending and axial compression [10,18]. Askarinejad et al. [17] tested whole internode sections of bamboo in torsion at varying degrees of environmental humidity, and found that the shear strain at failure increases with humidity (as in other plants) [20]. Samples conditioned at approximately 60% humidity had the highest average shear modulus and strength of 1.2 ± 0.35 GPa and 15 ± 8.6 MPa, respectively. Samples failed via brittle fracture consisting of a single crack propagating along the length of the internode. Their simulations revealed that the radial stiffness gradient of bamboo matches the stress gradient induced by torsion. The study did not reveal new micro or meso-structural adaptations, since the stiffness gradient documented had already been noted by several researchers [8,17,18,21].

In the southwestern deserts of North America one may find exquisite structures of hollow wooden cylinders, the walls of which are perforated by spiraling arrangements of holes (Fig. 1c, i). These are the remains of cholla cacti (genus *Cylindropuntia)*: spiny and ranging in size from shrub-like to 4.6 m tall, they are characterized by extensive cylindrical branches [22]. On death, the cholla leaves behind wooden "skeletons" of hierarchically porous hollow tubes sometimes used by artists to craft objects such walking sticks, chairs, and other furniture (Fig. 1c, ii) [23]. These skeletons are formed by the vascular cambium, a growth layer which produces xylem on the interior and phloem on the exterior. The xylem comprises thick cell walls reinforced by lignin, a highly branched and compressively stiff (but brittle) polysaccharide [24,25]. The support of lignin allows the xylem to conduct fluid and provide structural integrity for the phloem which comprises still living parenchyma responsible for nutrient storage and transport, lacking lignified cell walls [26]. A young cholla cactus forms a net-like series of vascular bundles with soft parenchyma cells in between, and as the cactus matures, the vascular bundles and bridges between them lignify to form the wood skeleton. The parenchyma cells in between remain unlignified, maintaining centimeters wide holes in the wood skeleton to maintain the succulence of tubercles (i.e. the fleshy projections tipped with spines). As the cactus grows taller, a new tubercle will grow roughly ~137 ° away about the vertical axis at a slightly higher position eventually resulting in a dense, spiral arrangement of tubercle pores shown in Fig. 1c, ii [23]. In some species such as *Cylindropuntia leptocaulis*, the holes are long and narrow, but in species with wide tubercles the holes are more circular [23]. Botanists have considered the positioning of these

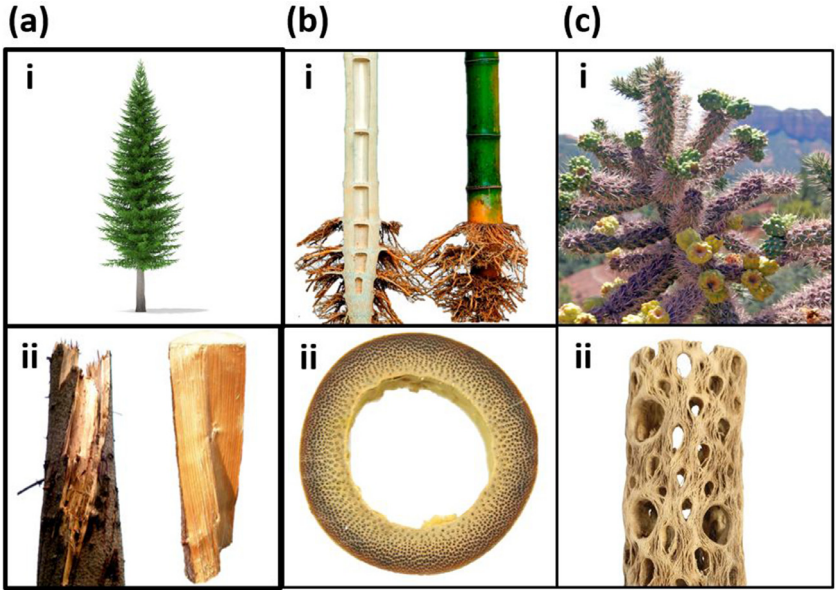

Fig. 1. The structure of natural materials are characterized by adaptations to mechanical loading. (a) (i) Norwegian spruce trees can grow spiraling grain to increase torsional strength in the direction of spirality [54]. (ii) Spiral handedness can differ from tree to tree depending on the prevailing wind direction [11,12,55]. (b) (i) The hollow of bamboo maximize its moment of inertia and beam-bending stiffness [56]. (ii) The macrostructure is augmented by the mesostructure of a radial density gradient of denser, stiffer tissue at the periphery, allowing rapid and material-efficient growth [18,57,58]. (c) (i) Cholla cacti grow in harsh, windy deserts of the North American southwest [59]. (ii) The fleshy, succulent tissue is supported by an internal lignified "skeleton" of wood with helical porosity. Previous work that examined the tubercle pores hypothesized they help optimize spine-packing density or thermal stability of the cactus [23,27]. Figures adapted from cited sources.

holes in context of the function of the tubercles: some hypothesize that they maximize packing efficiency of spines to protect the plant while minimizing interference [27], while others that they confer thermal stability against the extreme temperatures of the day and night of the desert [23]. Here, we explore the hypothesis that the positioning of the tubercle pores in the wood skeleton is an adaptation that confers density-efficient torsional integrity in a resource-sparse desert environment. As highly branched and squat plants, cholla are subjected to significant torsional loading compared to bending according to the geometric criteria developed by Skatter and Kucera [11,12]. The skeleton must confer enough torsional integrity to not only bear the weight of the cactus but also desert wind speeds of up to 28 m/s [28].

This work characterizes the macro-structure, meso-structure, and mechanical properties of the wooden cholla cactus skeleton from *Cylindropuntia acanthocarpa* (common names: staghorn or buckhorn stick cholla) via experimental techniques, and finite element analysis. The meso-structure of the wooden skeleton of *Cylindropuntia ramosissima* (common name: pencil cholla) was also characterized to investigate the level of detail captured by laser scanning. This different, smaller species of cholla was selected for the laser scanning technique due to the size limitations of the scanner.

2. Materials and methods

2.1. External mesostructure characterization

Eight dried specimens of staghorn cholla wood were obtained from the Superstition Mountains, AZ and locally in San Diego, CA; one specimen of pencil cholla wood was obtained locally in San Diego, CA, for external mesostructural characterization as received in dry conditions. A NextEngine 3D Scanner (Santa Monica, CA) was used to obtain the 3D model of a pencil cholla (n = 1 samples) via a laser array scanning the skeleton in parallel, each scan of which was then stitched in ScanStudio software (Santa Monica, CA). To solve the accuracy and resolution challenges of laser-scanning, another technique known as close range photogrammetry [29] was implemented on specimens of staghorn cholla (n = 8 samples) using a Sony Alpha a7II Digital camera (Tokyo, Japan) with a resolution of 24.3 effective megapixel, together with a Sony FE 90mm f/2.8 Macro Lens (Tokyo, Japan). The combination of the high-resolution camera and the macro lens allowed the acquisition of several hundred zoomed, high-resolution images of small regions of interest on the staghorn cholla surface. These images were then processed using Agisoft Metashape (St. Petersburg, Russia), a software specialized in photogrammetric processing of digital images for the generation of 3D spatial data. The average angle from the R-T plane between nearest neighbor tubercle pores ($\alpha°$) was then measured by "un-rolling" the 3D model using CloudCompare (Paris, France) to obtain a planar surface from the 3D cylindrical point cloud. These measurements were compared to $\alpha°$ values obtained by physical measuring the cholla cactus, by which pore dimensions were also obtained. The pitch (pore center-to-pore center distance), axial pore length ($L_{Pore,\,A}$), and tangential pore width ($W_{pore,\,T}$) were obtained as shown in Fig. 2a. The bulk sample density (ρ^*) was measured as that of a hierarchical cellular solid using the equation:

$$\rho^* = \frac{m}{L_A \pi \left(r_{outer}^2 - r_{inner}^2\right)} \tag{1}$$

In which L_A = the A length of the specimen, r_{outer} = the outer radius of the wood, r_{inner} = the inner radius of the wood, and m = the hydrated mass of specimens.

2.2. Internal mesostructure characterization

A section of staghorn cholla wood was cut from a dry stalk used in external mesostructural characterization, and the radial-tangential plane (wood endgrain) was examined by cutting and polishing the axial face using progressively fine-grit sand paper and then imaged in a Keyence VHX1000 optical microscope (Osaka, Japan). This was followed by sputter coating with iridium at 85 μA for 10 seconds to reduce charging using an Emitech K575X

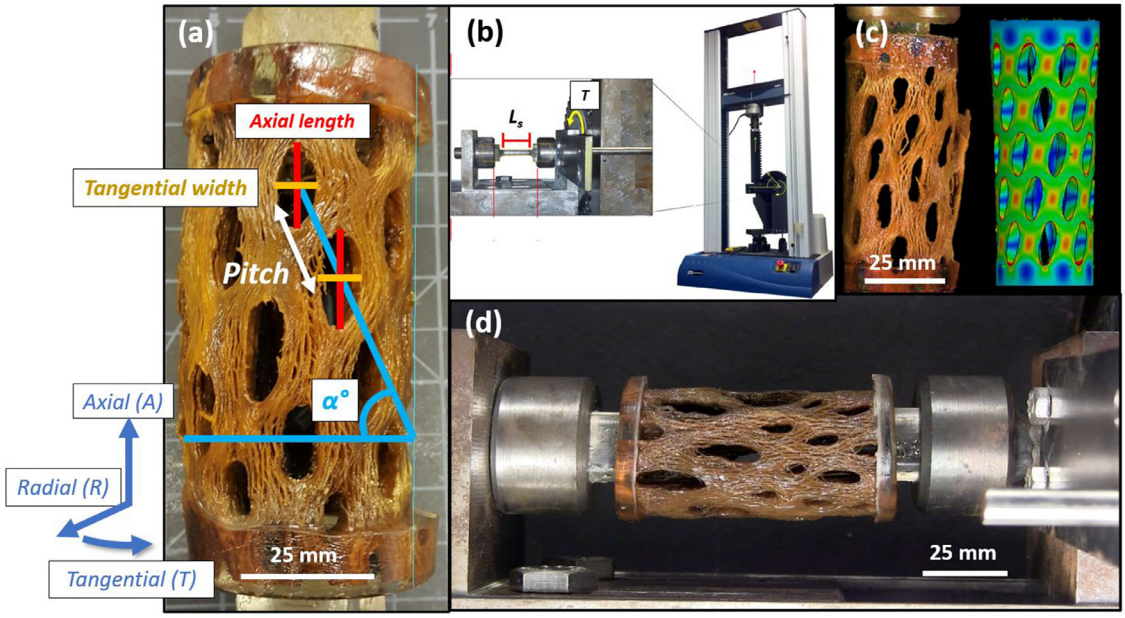

Fig. 2. (a) Manual measurements of the tubercle dimensions, pitch, and angle of orientation with respect to the radial-tangential plane were obtained for each cholla sample. Before testing, all specimens were fully hydrated to mimic *in vivo* conditions. (b) A torsional adaptor from previous work [30] was fitted to the Instron 3367 Dual Column Testing Systems device (Norwood, MA). It comprises a rack and a pinion that translates the vertical displacement of the Instron crosshead to torque on the sample. (c) To approximate the torsional moment (J_s) of each sample, a series of FEA models approximating the geometry of the cholla were generated and prescribed with isotropic steel parameters. Because J_s is a purely geometric constant, back-calculating G_{steel} provided an approximation applicable to the anisotropic cholla of similar geometry. (d) A hydrated cholla sample with epoxy reinforcements at each end, fitted into the torsion tester. Fig. adapted from cited source.

Sputter Coater (West Sussex, England). Samples were then imaged using the secondary electron detector of a Zeiss Sigma 500 field emission scanning electron microscope (SEM, Thornwood, NY) at an accelerating voltage of 2 keV and working distance of 10.4 mm. Unpolished, whole samples of cholla were also scanned in a Skyscan 1076 micro-computed tomography (μ-CT) scanner (Kontich, Belgium) both before and after mechanical testing to examine deformation mechanisms. The imaging was performed at 35 μm isotropic voxel size for gross scans and 9 μm voxel size for finer scans.

2.3. Torsion testing

From the eight large stalks of staghorn cholla received for mesostructural characterization, ten samples of staghorn cholla wood were cut into segments of varying length (13-18 cm) to maximize the number of straight-edged cylinders that could be obtained from the curved bulk material. After measuring the dry weight, length, inner radius, and outer radius of each sample, the cholla were hydrated for a week in water to mimic in vivo conditions of being surrounded by succulent cactus tissue which is typically ~80-95 wt.% water [23]. Following hydration, the samples were re-measured to obtain hydrated mass and the length (L), inner radius (r_{inner}), and outer radius (r_{outer}) of each sample. The end of each cylinder was then reinforced with 25 g of epoxy in a dog-bone mold (Fig. 2a) to allow samples to be secured to a custom built torsion testing device (Fig. 2b) [30] mounted to an Instron 3367 Dual Column Testing Systems device (Norwood, MA). The custom built device translated a linear displacement rate of 0.02 mm/s to a torsion rate of 2.0×10^{-4} radians/s, and the raw load v.s. displacement data were translated into torque v.s. rotation data and then shear stress v.s. shear strain, according to the procedures described by Porter et al. [30]. The calculation of shear stress required the sample torsional moment of inertia (J_s) which quantified the cross-sectional geometric resistance to twisting. Rather than estimate sample torsional moment of inertia as that of a hollow tube, J_s of each sample was obtained via generating $n = 9$ models in finite element analysis that approximate the range of geometries to obtain a J_s surface profile, the process of which is described in section 2.4. A comparison of a typical cholla sample to the average geometry as represented in FEA is shown in Fig. 2c. To compare the hydrated cholla torsional mechanical behavior to that of other biological materials, the shear strain results of whole bamboo internode culms conditioned in 100% humidity were taken from Askarinejad et al. [17]. The literature values were normalized by bulk density, which were not reported by Askarinejad et al. but could be inferred from the sample dimensions of the internode sections tested: Amada et al. [31] have previously determined a relationship between culm width and length and the culm number, which in turn determines bulk density. Literature values of physiologically hydrated bovine trabecular bone under torsion were taken from Fatihhi et al., which provided sample dimensions and density [32]. Five samples of balsa wood (Ochroma pyramidale) were also tested in torsion alongside the staghorn cholla samples. Balsa was chosen due to its highly hydrated physiological state, providing a similar wooden material of different macrostructure for comparison [33]. The 12 w.t.% moisture content balsa was obtained from National Balsa (Ware, MA) and prepared as cylindrical samples ($L = 62$ mm, $r = 16.45$ mm) cored from the centers of plain-sawn planks to obtain radial symmetry. The cylinder length corresponded to the axial direction. As with the cholla samples, the end of each cylinder was reinforced with 25 g of epoxy in a dog-bone mold, after which the samples were fully hydrated to reflect physiological conditions.

2.4. Finite element analysis (FEA)

Finite element analysis (FEA) in SolidWorks was employed to (1) approximate the J_s of each physically tested sample, (2) understand the stress concentrations caused by torsional loading and axial loading in isolation, and (3) investigate how the pore geometry affects the cholla cactus mechanical properties. To the first end, an

Table 1
Gibson-Ashby equations for anisotropic material properties [10].

Property	Direction of loading		
	Tangential	Radial	Axial
Young's modulus	$\frac{E_T}{E_s} = 0.54\left(\frac{\rho^*}{\rho_s}\right)^3$	$\frac{E_R}{E_s} = 0.8\left(\frac{\rho^*}{\rho_s}\right)$	$\frac{E_A}{E_s} = \left(\frac{\rho^*}{\rho_s}\right)$
Shear modulus	$\frac{G_{RT}}{E_s} = 0.074\left(\frac{\rho^*}{\rho_s}\right)^3$		$\frac{G_{AT}}{E_s} = \frac{G_{AR}}{E_s} = 0.074\left(\frac{\rho^*}{\rho_s}\right)$
Poisson's ratio	$\nu_{TR} = 1$ $\nu_{TA} = 0$	$\nu_{RT} = 1$ $\nu_{RA} = 0$	$\nu_{AR} = \nu_{AT} = \nu_s$
Crushing strength	$\frac{\sigma_T}{\sigma_{y,s}} = 0.14\left(\frac{\rho^*}{\rho_s}\right)^2$	$\frac{\sigma_R}{\sigma_{y,s}} = 0.20\left(\frac{\rho^*}{\rho_s}\right)^2$	$\frac{\sigma_A}{\sigma_{y,s}} = 0.34\left(\frac{\rho^*}{\rho_s}\right)$
Shear strength	$\frac{\tau_{RT}}{\sigma_{y,s}} = C\left(\frac{\rho^*}{\rho_s}\right)^2$		$\frac{\tau_{AR}}{\sigma_{y,s}} = \frac{\tau_{AT}}{\sigma_{y,s}} = 0.086\left(\frac{\rho^*}{\rho_s}\right)$

initial cholla cactus-like model was developed using average relative dimensions of pore geometry and wall thickness. Then, maintaining constant single pore area and cactus outer diameter while varying pore circularity and stalk wall thickness-to-outer diameter ratio, a total of n = 9 models were generated. The pore circularity and the wall thickness-to-outer diameter ratio were varied each had three levels of 0.98, 0.78, and 0.54 and 0.0811, 0.135, and 0.189, respectively. Pore circularity was defined as:

$$Circularity = 4\pi \frac{(pore\ area)^2}{(pore\ perimeter)^2} \tag{2}$$

In which a perfect circle has a circularity = 1. The pore circularity = 0.78 was based on the average measurements of pore pitch, $L_{\text{pore, A}}$ and $W_{\text{pore, T}}$, and α° collected from several specimens. The wall thickness-to-outer diameter ratio of 0.135 was similarly based on average measurements. The bulk material for the models was simulated as isotropic steel with $E = 210$ GPa and $\nu = 0.3$ and was subjected to torsion with torque (T) in the elastic regime with one fixed end. From the angular displacement (ϕ) and known shear modulus, G, an approximation of J_s (which is a strictly geometric parameter) was obtained using the below equation for the torsional deflection of a circular shaft:

$$\phi = \frac{LT}{J_s G} \tag{3}$$

From the resulting surface profile of J_s values, the torsional moment of physical samples were approximated based on their pore circularity and wall-to-outer diameter ratio.

To the second aim of understanding stress concentrations caused by torsional loading and axial loading separately, it was necessary to obtain material parameters of the anisotropic cholla wood. Using the density of the dry cholla wood, an initial set of estimates for Young's moduli (E_A, E_R, E_T), shear moduli (G_{AR}, G_{RT}), crushing strength ($\sigma_{\text{c, A}}$, $\sigma_{\text{c, R}}$, $\sigma_{\text{c, T}}$), tensile strength ($\sigma_{\text{t, A}}$, $\sigma_{\text{t, R}}$, $\sigma_{\text{t, T}}$), mode I fracture toughness ($K^*_{\text{IC, A}}$, $K^*_{\text{IC, RT}}$), and Poisson's ratios (ν_{AR}, ν_{TR}) were obtained via Gibson-Ashby equations summarized in Table 1 [10]. These values were then adjusted for their moisture content [20] using the equation:

$$P = P_{12}\left(\frac{P_{12}}{P_g}\right)^{\frac{12-M}{M_P-12}} \tag{4}$$

In which P = property at moisture content M, P_{12} = property at 12% moisture value (obtained using Gibson-Ashby equations), $M_{\text{P}} = 25$ (fiber saturation point), and M = moisture content as calculated by:

$$M = \frac{mass_{dry} - mass_{wet}}{mass_{dry}} * 100\% \tag{5}$$

The moisture-adjusted material parameters were then input into FEA simulation. For each set of material parameters, three simulations were run with prescribed torque corresponding to three values of shear stress in the linear elastic range of an experimental curve. Simulation material properties were adjusted iteratively and in proportion to one another according to Gibson-Ashby equations until the three points produced a shear stress-strain slope matching the average experimental slope. Stress concentrations of this model were examined in torsion and in axial loading.

Finally, to the third aim of understanding how pore geometry affected the cholla mechanical properties, the material parameters obtained in the second aim were applied to all n = 9 models described in the first aim. All models were again prescribed axial compression and torsion separately within the elastic regime, with one fixed face. The ratios of the effective axial modulus to material axial modulus and effective shear modulus to material shear modulus were then compared.

3. Results & discussion

3.1. External mesostructure characterization

Despite its high cost, the laser scanner only captured the pencil cholla's tubercle pores without the complexity of its fiber orientations (Fig. 3a). On the other hand, the photogrammetry-produced model of the staghorn cholla more accurately reflecting the natural material and captured the tubercle pores and fiber protrusions and troughs (Fig. 3b). The photogrammetric model clearly showed how fibers grow axially and diverted around, wove between, or split into smaller fibers at a tubercle pores seemingly at random, as illustrated in the magnified portion of Fig. 3b. One growth step may not dictate the next: a fiber may weave between pores only to split into smaller fibers at the next. Analysis of the "unrolled" staghorn cholla model produced lower angle measurements (50 ± 1.5 °) compared to the physical measurements (65 ± 2.1 °). The digital measurements from the photogrammetric model provided the line of best fit through several tubercle pores whereas the physical measurements were obtained only by considering nearest neighbors, and so provided more accurate information of the geometry of the cactus. Because of its low-cost and ease of use, pho-

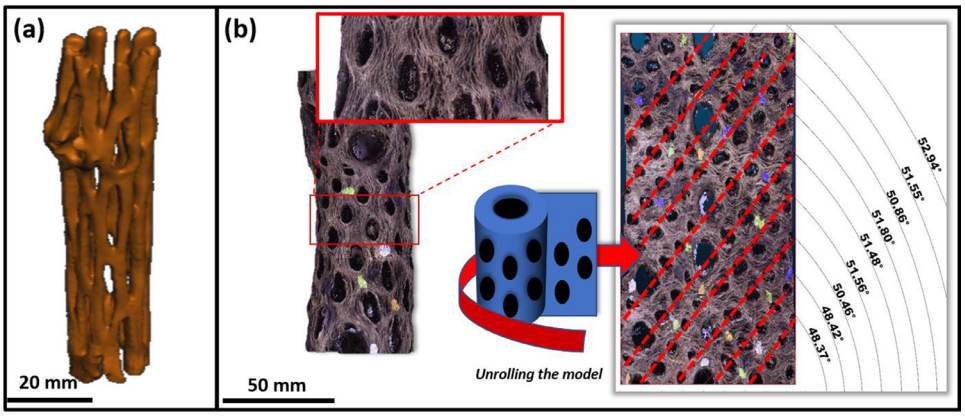

Fig. 3. (a) Though useful for creating 3D models that capture the general shape of a biological structure, the laser scanner was unable to capture the fiber complexity of the pencil cholla skeleton imaged. (b) The photogrammetric model successfully captured the fiber complexity of the staghorn cholla. By "unrolling" the model in MATLAB, a more accurate assessment of overall tubercle arrangement could be obtained than by hand measurements: lines can be drawn (red, dashed) through the centers of tubercle pores to examine the overall growth pattern (i.e. angle of orientation with respect to the radial-tangential plane) rather than neighbor-to-neighbor comparisons as was done manually (Fig. 2a).

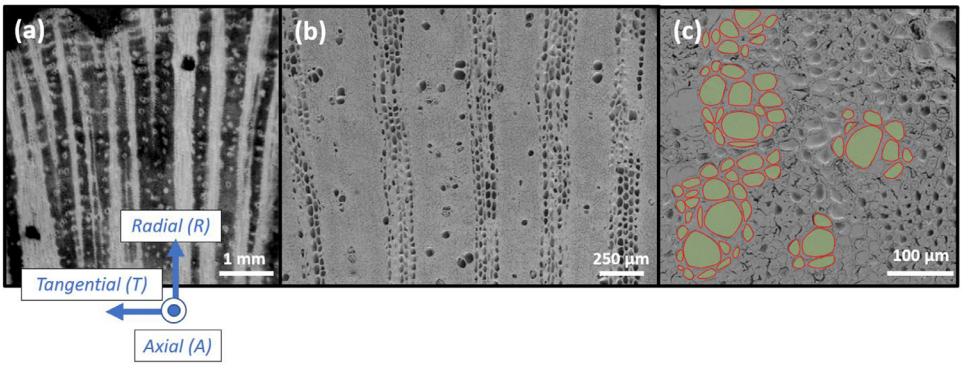

Fig. 4. (a) The endgrain of the cholla cactus as observed in optical microscopy features aggregate rays and a diffuse-porous arrangement of vessel elements. (b) The same face examined in scanning electron microscopy shows relatively small but numerous vessels to allow maximum axial conduction of water during intermittent rain while preventing cavitation during dry seasons [48]. The similar ray cells conduct water to fleshy succulent tissue for storage, and can store water themselves [49]. (c) Clusters of vessels are highlighted in green, distributed amongst tracheids.

togrammetry presented a powerful method in 3D characterization of biological materials.

3.2. Internal mesostructure characterization

Polished cross sections of the cholla endgrain (Fig. 4a, b) revealed a conventional wood mesostructure that can be described using categories developed by the International Association of Wood Anatomists (IAWA) [34]. The large, thin-walled tubules are vessels responsible for axial nutrient conduction and are dispersed uniformly in a diffuse-porous arrangement. The alternating bands of light and dark wood visible in the optical microscope correspond to bands of aggregate rays and tracheids, respectively.

Gross µ-CT (voxel size = 35 µm) revealed that like other woods, cholla was characterized by alternating rings of light "earlywood" (colorized in blue in Fig. 5a) and denser "latewood," (colorized in green in Fig. 5a) which correspond to faster growth during the spring and summer and slower growth during cool autumn and winter. As observed from photogrammetry, the fibers in the staghorn cholla diverted around, wove in between, or split into smaller fibers at tubercle pores (Fig. 5b). Compared to the photogrammetry scan however, it was observed visually that the fibers were more densely packed in the interior with fewer voids in between than at the surface, consistent with their growth pattern discussed in the Introduction.

Slowly raising the density threshold (Fig. 5c, i–iii) exposed a network of discontinuous "islands" of heavily lignified tissue embedded in the xylem in between the tubercle pores, in the "ligaments." Unlike in bamboo, which exhibits radial density gradients [18], the islands appeared to be radially continuous, indicating that points of reinforcement were consistent over time (Fig. 5c, iii). The tubercle pores edges were only somewhat discernable at the highest density threshold, indicating that the ligaments were preferentially reinforced (a point that we note for discussion in the results of the finite element model of the cholla in torsion, Section 3.4).

3.3. Torsion testing

Staghorn cholla shear stress-strain curves consistently exhibited a linear regime followed by a decreasing, jagged plateau under torsion. The average shear modulus and strength (n = 8) were found to substantially vary at 41 ± 7.8 MPa and 2.7 ± 1.0 MPa, respectively, but when normalized by hydrated bulk density showed more consistent behavior, typical of woody structures: the specific effective shear modulus, $G/\rho^* = 150 \pm 23$ MPa $(g/cm^3)^{-1}$ and the specific shear strength, $\sigma_y/\rho^* = 9.3 \pm 2.5$ MPa $(g/cm^3)^{-1}$. Most notably, the toughness was strikingly high (1100 ± 430 kJ/m^3). Plotting the density-normalized behavior of cholla allowed comparisons to balsa wood, bamboo, and trabecular bone as well as account for sample-to-sample variation (Fig. 6). Though its curve profile was similar to the cholla cactus, hydrated balsa exhibited a far lower density normalized shear stiffness, strength, and toughness indicating low mechanical efficiency. Failure occurred via a single oblique fracture plane 45° to the axial length of wood. The

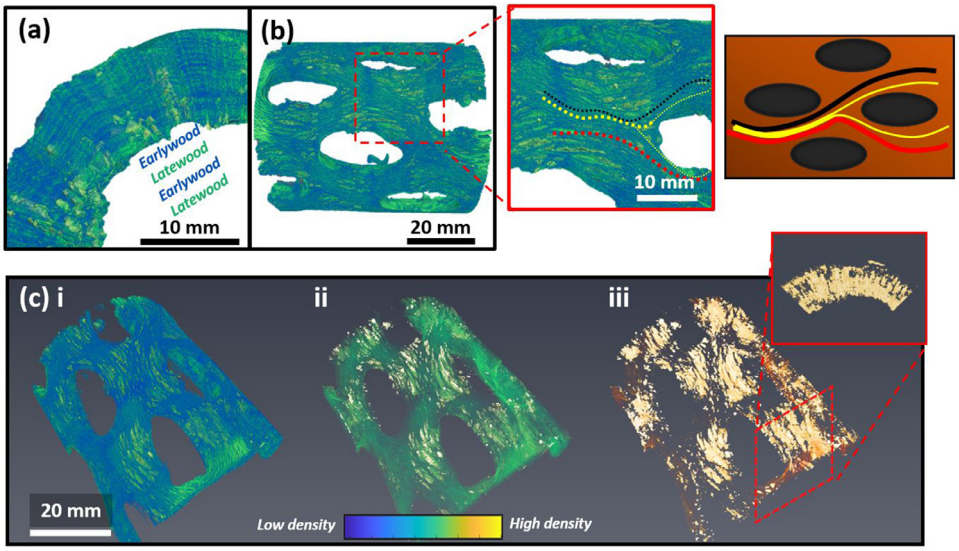

Fig. 5. μ-CT of a specimen revealed (a) banding of latewood and earlywood in the radial-transverse plane, corresponding to slow and fast growth periods respectively. (b) Fibers were observed to weave in between, divert around, or split off into smaller fibers at tubercle pores. (c) Slowly raising the density threshold progressively from (i—iii), radially continuous regions of increased lignification were observed, mainly at the tubercle ligaments.

Table 2
Summarized torsional properties.

Material (in physiological conditions)	**Effective shear modulus**		**Torsional strength**		**Torsional toughness**
	(MPa)	$(\frac{MPa}{g/cm^3})$	*(MPa)*	$(\frac{MPa}{g/cm^3})$	(kJ/m^3)
Staghorn cholla (n = 8)	41 ± 7.8	150 ± 23	2.7 ± 1.0	9.3 ± 2.5	1100 ± 430
Balsa wood (n = 5)	33 ± 4.6	31 ± 3.7	1.7 ± 0.64	1.6 ± 0.33	160 ± 12
Bamboo culm	470	550	9.4	11	350
Trabecular bone	63	57	4.5	4.1	540

density normalized shear modulus of the bamboo was greater than that of the cholla ($G/\rho^* = 550$ MPa $(g/cm^3)^{-1}$), but its strength comparable (11 MPa $(g/cm^3)^{-1}$) and toughness less than half (350 kJ/m^3). Bamboo's ultimate failure strain occurred at less than 0.06, a full order of magnitude below that of cholla, and was characterized by a single axial crack propagating along the entire length of the bamboo internode culm [17]. Fatihhi et al. [32] showed trabecular bone's G/ρ^* to be comparable to that of cholla but with lower σ_y/ρ^*. Like cholla, trabecular bone exhibited torsional toughness but failed at a shear strain of 0.2—though Fatihhi et al. did not report how trabecular bone failed under pure monotonic torsion, Bruyere-Garnier et al. [35] reported that torsion induced an oblique fracture plane 45° to the axial length of trabecular bone. Thus, while torsion in bamboo generated shear failure (creating A-R plane cracks), in balsa and trabecular bone the tension caused by torsion resulted in a tensile failure oriented 45° to the A axis. The properties of each material were summarized in Table 2.

That cholla, like balsa and bone, decomposed torsion into tension and compression is key to its high toughness. As evidenced by the sequence of deformation in Fig. 6c, initially elliptical tubercle pores were compressed tangentially and stretched axially at a coordinate offset of 45° to the A axis of the plant, prior to tensile failure in which fibers ruptured. The difference between bamboo (shearing decomposition) and balsa and cholla (tensile and compressive decomposition) was that the fibers in the latter were highly saturated with water, reducing the stiffness and strength of the wood [36]. Water hydrated the hemicellulose matrix between fibers and facilitated inter-fiber sliding while retaining some stiffness via constant breaking and reforming of hydrogen bonds [24,37,38]. With less moisture in their physiological state, bamboo fibers were over-adhered to one another and unable to bend or slide past one another. Instead, they failed at their interfaces to produce clean A-R plane cracks. The balsa fibers were clearly able to bend and slide, but due to their lower density cell walls and higher state of hydration exhibited lower mechanical efficiency. Bone is a markedly different material than wood, but according to literature deforms via a similar flowing mechanism between mineralized collagen fibrils in its hydrated physiological state—the fibrils themselves and the mineral platelets experience very little deformation [37].

The unique deformation mode in cholla was due to the hierarchical arrangement of fibers which is quite different from balsa, in

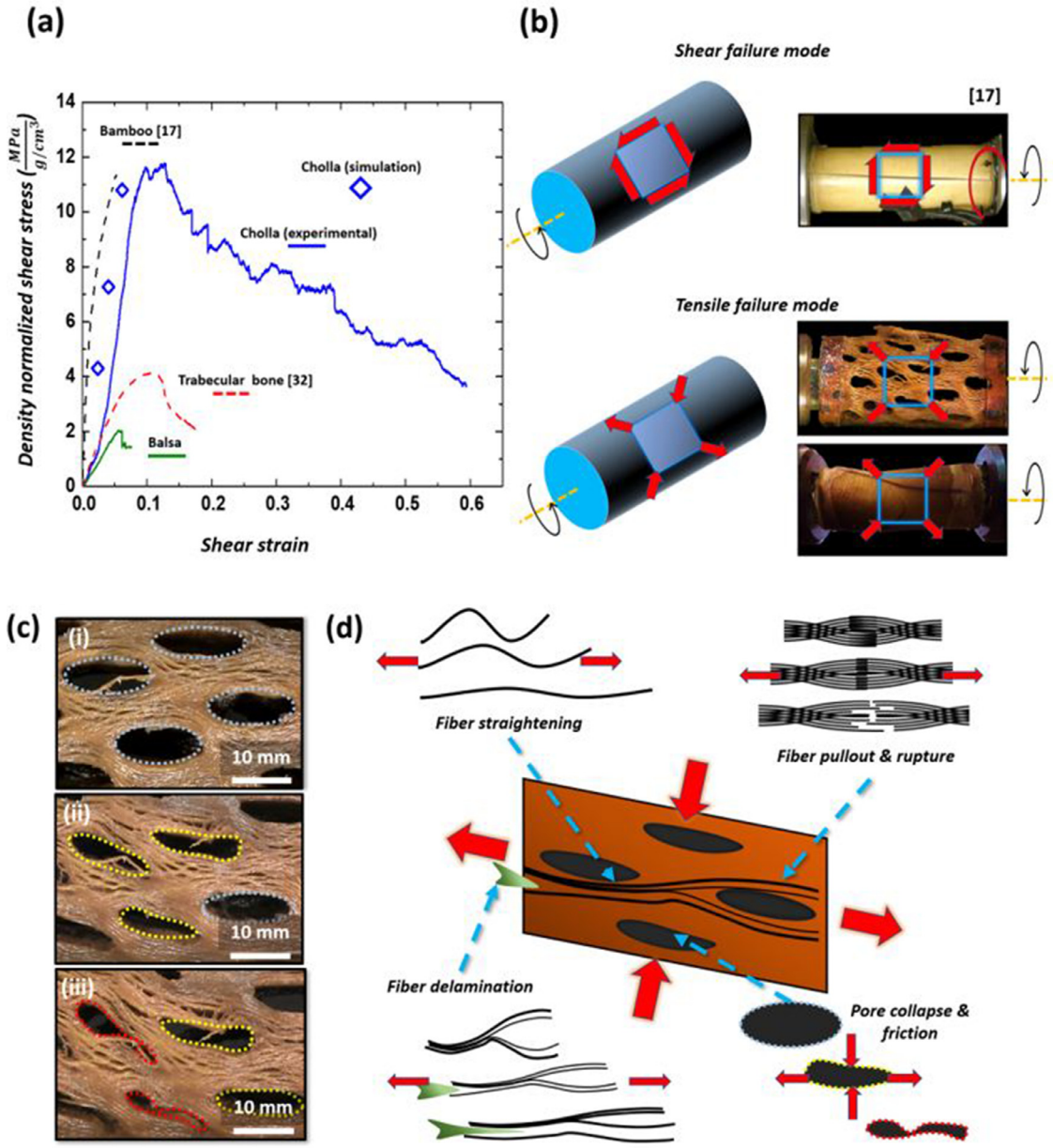

Fig. 6. (a) Compared to the density-normalized performance of bamboo [17], balsa, and trabecular bone [32], cholla exhibited a far greater combination of stiffness, strength, and toughness. (b) While bamboo decomposed torsion into shear as evidenced by its failure mode (adopted from [17]), cholla, balsa, and trabecular bone decomposed torsion into a combination of tension and compression. (c) That cholla decomposed torsion into tension and compression was especially evident by examining the elongation and flattening of the tubercle pores. (d) Several mesostructural deformation mechanisms contributed to the highly tough torsional behavior. Figure adapted from cited source.

spite of similarities in composition and hydration. The cholla's hydrated material properties determined four mesostructural deformation mechanisms illustrated in Fig. 6d: fiber straightening, fiber delamination, pore collapse and friction, and ultimately fiber rupture and pullout. As noted in Fig. 5b, the cholla fibers grew in serpentine paths in the axial direction. As the wood began to plastically deform in torsion, individual fibers were elongated in the direction of tension and absorbed energy via straightening and then elastic stretching of the fiber itself. As the fibers straightened, however, they separated from neighboring fibers and further energy was absorbed via delamination. All the while, the macroscopic tubercle pores were flattened by the compressive force in the perpendicular direction until they collapsed. Like the densification effect of a cellular solid under compression, each collapsed tubercle pore newly offered compressive and frictional resistance under torsion. The pores did not deform simultaneously but sequentially from the loading face. Once the fibers were fully straightened in tension at an extreme shear strain (~0.6), an energy-absorbing fiber failure occured in the R-T plane. At this point the cholla lost its cylindrical shape as sections of the wall twisted inward, but even then the wood did not catastrophically fail and still retained some stiffness. Due to the sequential nature of the post-elasticity in cholla torsional deformation, these four mechanisms (fiber straightening, fiber delamination, pore collapse and friction, and fiber rupture and pullout) happened in parallel and avoided catastrophic failure, resulting in a gradual decrease of torsional load.

Compared to other biological materials, it was this toughness that was most striking. As previously discussed, the squat and branched geometry of the cactus creates a strong evolutionary pressure to adapt accordingly for torsion. The question remains, however, on why toughness was seemingly prioritized. High stiff-

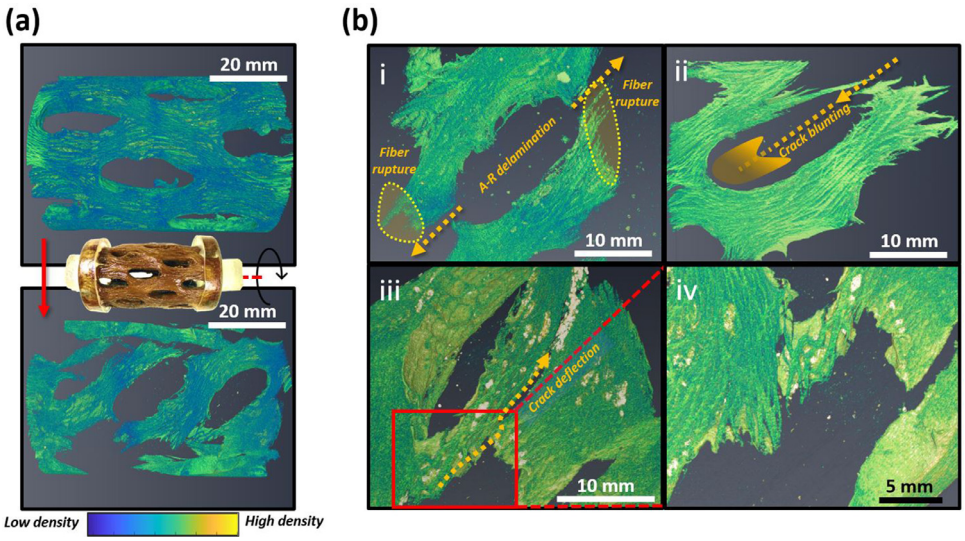

Fig. 7. (a) Micro-computed tomography images of a specimen (i) before and (ii) after torsion revealed several extrinsic toughening mechanisms. (b) (i) Fiber rupture of the wood showed signs of highly energy absorbant progressive delamination. (ii) A-R delamination was blunted by tubercle pores, slowing its advance. (iii, iv) Alternatively, the weaving and criss-crossing fibers would divert the A-R delamination on a still more tortuous path.

ness and strength would require either devoting more bulk material growth to the plant or increased lignification. In a resource poor environment, these may not be feasible. Alternatively, reduced hydration stiffens and strengthens the stalk, but this may interfere with other biological functions of the plant. Additionally, a lower fiber hydration embrittles the wood as in bamboo, making catastrophic A-R failure more likely from which recovery would be near impossible [39]. It may be that the cactus' primary response to torsion in a non-catastrophic, localized, and staggered failure sequences helps it to recover from damage and uses resources most sparingly. Rather than regrow entire sections of plant or heal massive cracks spread throughout the plant, it is more efficient to seal and regrow smaller, distributed delaminations [39,40].

Micro-CT images of the cholla after torsion (Fig. 7a) showed further detail in the tensile fiber failure: in Fig. 7b, i, fiber rupturing was shown to be caused by fiber pullout in a mixture of delamination and tensile fiber failure. This mode is known as "progressive delamination" in the field of composite failure and describes optimally adhered fibers that are neither over nor under adhered to allow maximum energy absorption in failure [41]. In some cases this delamination terminated at another tubercle pore in a process akin to crack blunting (Fig. 7b, ii), while in others the delamination was diverted around a neighboring tubercle. This was determined by whether the fibers along which the crack propagated diverted around, wove between, or split into smaller fibers at a tubercle pore. In Fig. 7b iii & iv, for example, the criss-crossing of fibers deflected an incoming crack to force a more tortuous path. All these mechanisms enhanced the torsional toughness of the cholla.

3.4. Finite element analysis (FEA) Simulation

FEA was implemented with three aims: (1) to capture the variation of torsional moment J_s (with parameters of pore circularity and stalk wall thickness-to-diameter), from which torsional stress was calculated, (2) to understand stress concentrations caused by torsional and axial loading acting separately on cholla models with appropriate anisotropic wooden material parameters and (3) to understand the effect of pore geometry and wall thickness-to-diameter ratio on the cholla's ability to resist torsional and axial loads. Boundary conditions were validated by simulating solid-walled tubes with isotropic steel parameters and back-calculating input material parameters.

While the first aim was a means to analyze experimental data, the second and third aims provided significant insight into the material behavior of the cactus. By inputting a relative density of 0.15 into equations summarized in Table 1 and adjusting with $M = 25$ % according to Equation 4, an effective shear modulus (i.e., the slope of the three simulated shear stress-strain values) within 10% of the experimental shear modulus was obtained, the results of which are shown in Fig. 6a. Because the Gibson-Ashby equations were not meant to calculate precise mechanical properties from relative density but rather estimates, it was not a significant discrepancy that the average cholla relative density was in fact 0.23 ± 0.017 [10]. It should be re-emphasized that the average experimental "shear modulus" calculated using Equation 3 ($G_{\text{effective, experimental}} = 41 \pm 7.8$ MPa) represented the tube's resistance to torsion and not its material shear stiffness. As discussed in Section 3.3, the torsional shear can be decomposed into tensile and compressive loads acting at ± 45° to it. The cholla wood's true shear stiffness is likely $G_{\text{A-R, material}}$ ~ 340 MPa which was input into the material simulation to obtain $G_{\text{effective, simulation}} = 50$ MPa shown in Fig. 6a. Because all material properties were simultaneously adjusted using relative density for the simulation, it is possible that in the actual wood some properties were separately higher or lower than the relative values predicted by the Gibson-Ashby equations (i.e. the wood's shear stiffness may be lower than the Gibson-Ashby equations predict, while the wood's axial stiffness may be higher).

With anisotropic material parameters verified against experimental results, it was possible to examine stress concentrations produced by torsional and axial loading. It was clear that torsion produced stress concentrations in the middle of the ligaments between tubercle pores (Fig. 8a, i), while axial compression produced stress concentrations at the axial ends of the tubercle pores (Fig. 8a, ii). The regions of heavy lignification observed in μ-CT (Fig. 5c, iii) matched the points of stress concentration in torsion rather than compression. Because woody plants reinforce branch junctures [42], taproots [43], and other stem portions [8,43–46] in response to mechanical stress, it is likely that cholla selectively increased lignification to create a mechanically efficient stalk of high torsional stiffness.

The models in Fig. 8a represented the average geometries of the measured cholla: to investigate the effect of the pore geometry on the cactus, pore circularity and stalk wall thickness-to-diameter

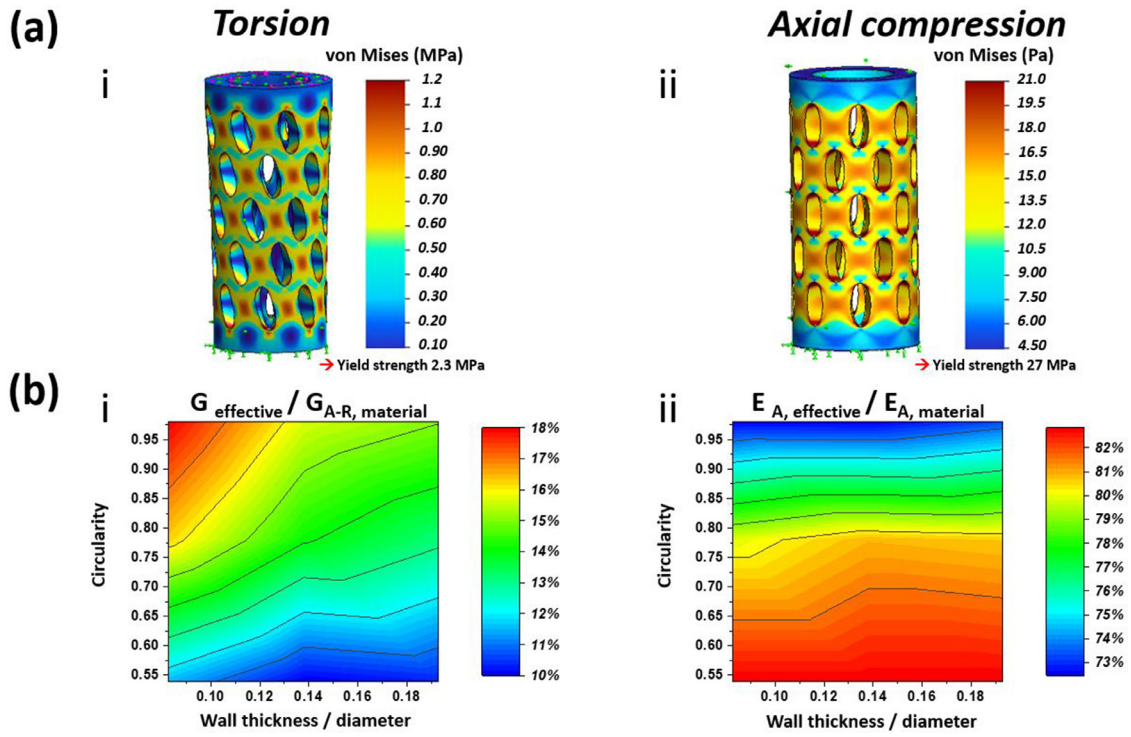

Fig. 8. (a) Finite element analysis (FEA) was used to model an average cholla sample in (i) elastic torsion and (ii) compression using anisotropic material parameters validated by comparison to experiments in Fig. 6a. It was clear that regions of heavy lignin self-reinforcement observed in Fig. 5c, iii corresponded to torsional stress concentrations in the ligaments between pores. (b) By plotting the ratio of the effective stiffness to the prescribed material stiffness in (i) torsion and (ii) compression, it was observed that the cholla pore geometry confers a compromise between torsional and axial stiffness.

ratio were varied with three levels each. The centers of the heat maps of Fig. 8b reflect the average cholla pore circularity and wall thickness-to-stalk diameter ratio, while the color intensity reflects the effective stiffness as a percentage of the prescribed material stiffness. It was observed that for thin walled tubes, a higher pore circularity improved the effective shear stiffness whereas in thicker walled tubes there were diminishing returns past circularity ~ 0.65 (Fig. 8b, i). In axial loading, the wall thickness-to-diameter ratio had little effect on the effective compressive stiffness while a lower pore circularity improved the effective stiffness (Fig. 8b, ii). At approximately the average geometry of the staghorn cholla there was a balanced compromise between the effective axial and shear stiffnesses, indicating that the macrostructure of the cholla is an adaptation to bear both torsional loads due to wind and axial load due to its own weight. As observed in Fig. 2d, however, cholla pore geometry can vary even on a single stalk—it may be that a cholla cactus can locally adjust pore roundness as a mechanism to control its stalk stiffness.

This FEA analysis was limited, however, in that staghorn cholla wood may be optimized simultaneously for several factors such as other loading modes (e.g. radial compression due to tissue swelling, bending) and biological functions. For example, plant xylem is responsible for nutrient and fluid conduction which are of particular importance in the desert, where cacti must be able to rapidly take-up liquid during rare instances of rain fall [47]. Unique adaptations to this end have been observed at all hierarchical levels of cacti: these include a shallow, spreading root system (ideal for transient rainfall) [23], a relatively thin living-cell layer in the roots to maximize axial conduction [47], small and numerous vessels in the stem to maximize conduction and prevent cavitation during drying [48,49], and larger vessels at the root-stem juncture to induce air bubbles and prevent water loss from the succulent stem into the dry soil [47]. It is possible that too oblique a mesopore distribution in the wood (i.e. too oblique a fiber angle of the wood that must wrap around them) interferes with this critical function of xylem, explaining why the cholla cacti mesopores are distributed at an angle greater than 45 °. Another example of a biological function that our analysis did not account for is spine distribution (each tubercle pore corresponds to the placement of spines). We have already mentioned the theory that the helical geometry of the tubercles allows maximum packing density of spines while minimizing spine overlap for efficient protection against would-be water thieves [27]. Another function of the spines, however, is to collect moisture from air and transport droplets by their aligned grooves to fine, water-absorbing outgrowths at the spine base (trichomes) [50]. The mesopore distribution may optimize for spine packing efficiency not just for protection but water condensation, too. A final, major biological function unaccounted by our analysis is that of the surrounding living tissue: compared to the parenchyma of conventional plants, the parenchyma of cacti are extremely hydrated. The elastic yet strong bark combined with this succulence confer high turgor pressure which substantially augments the cactus' mechanical properties [51–53]. The results of our FEA show a compromise between torsional and axial loading of the cholla wooden frame, but can provide only a partial insight as to the evolutionary reasons for the cholla's mesopore distribution.

4. Conclusions

To understand how cholla cacti withstand torsion induced by high desert winds, specimens of staghorn cholla were characterized using photogrammetry, optical microscopy, and scanning electron microscopy (SEM), and then hydrated and tested in quasi-static torsion. Photogrammetry proved to be a cost-efficient method of producing a 3D model relative to laser-scanning that could still capture fine features such as fiber orientation, while SEM revealed a conventional diffuse-porous and ag-

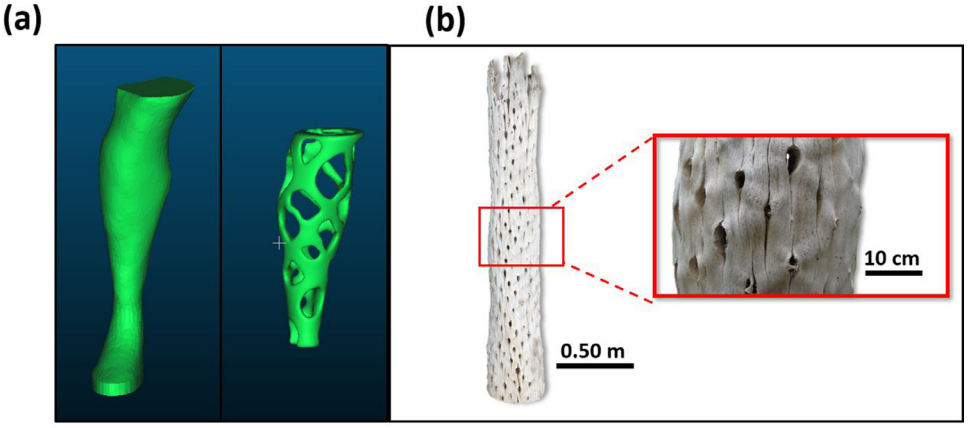

Fig. 9. (a) Cholla inspired hierarchical architecture such as optimally adhered fibers, fiber-criss crossing, and helical macroporosity may be combined to inspire light, torsionally stiff and tough composites. Applications could include prosthetics or next-generation driveshafts where catastrophic failure is highly undesirable. (b) The approach used in this study may be applied to distantly related desert plants such as *Fouquieria columnaris* which exhibit signs of convergent evolution.

gregate ray wood mesostructure. Specimens tested in torsion exhibited density-normalized torsional stiffness and strength comparable to that of bamboo, but their most remarkable property was their toughness (1100 ± 430 kJ/m^3) far exceeding that of other biological materials. The cholla's highly hydrated physiological state allowed the wood material to decompose the torsion into tension and compression rather than shear via fibril sliding and bending. These material properties were further enhanced by the mesostructural deformation mechanisms that absorbed high amounts of energy. Post-damage characterization in μ-CT revealed that fiber rupture occurred via progressive delamination, and that crack blunting by tubercle pores and winding fiber growth impeded delamination in the A-R plane.

FEA revealed how the cholla pore geometry provided a compromise of density-efficient axial compressive stiffness and torsional stiffness, while μ-CT revealed how regions of lignification matched FEA stress concentrations under torsion. These were our major findings:

- Cholla's physiological hydration reduced torsional stiffness by allowing fibril sliding and bending, but in turn improved toughness.
- These material properties were hierarchically complemented by mesostructural deformations of fiber straightening, fiber delamination, pore collapse and friction, and ultimately fiber rupture via progressive delamination.
- FEA demonstrated that pore geometry macrostructure provided a balance between torsional and axial stiffness, highlighting the need for the cholla to resist twisting forces while supporting its own mass.
    - Torsional loading stress concentrations in FEA corresponded to regions of extensive lignification in the cactus, demonstrating a feedback between local material properties and macroscopic structure.

The mesostructural features identified in this paper may be translated into bio-inspired designs, particularly with fiber-laminate composites that could combine the cholla's use of geometry and fiber-toughening mechanisms. In drive-shafts or lower limb prostheses for example, cholla-inspired helical porosity can be implemented via topology optimization while also using winding fiber patterns to create torsionally stiff, strong, and tough columns using minimal material (Fig. 9a). Furthermore, a similar approach as this study may be used to examine species such as the cirio tree (*Fouquieria columnaris*) shown in Fig. 9b. This North American desert plant, only distantly related by clade, grows its wood with a helical porosity that hints at convergent evolution in the Sonoran desert. Future work should investigate how topology optimization and FEA could be used to investigate the fiber orientations of the cholla cactus, and provide a more complete picture of how stresses are distributed in the natural material. Additionally, fiber composites may be fabricated mimicking the cholla structure while tuning adhesion, pore geometry, pitch, and angle to determine how desirable mechanical properties and failure modes may be obtained. Alternatively, cholla-like structures may be explored via multi-material 3D printing. These would present the added benefit of being able to mimic the cholla's local stiff inclusions and fabricate more complex and varying pore geometries.

Declaration of Competing Interest

The authors declare that they have no known competing financial interests or personal relationships that could have appeared to influence the work reported in this paper.

Acknowledgements

This work is supported by a Multi-University Research Initiative through the Air Force Office of Scientific Research (AFOSR-FA9550-15-1–0009) and a National Science Foundation Biomaterials Grant (1507978). This work was performed in part at the San Diego Nanotechnology Infrastructure (SDNI) of UCSD, a member of the National Nanotechnology Coordinated Infrastructure, which is supported by the National Science Foundation (Grant ECCS-1542148).

References

[1] L.K. Grunenfelder, N. Suksangpanya, C. Salinas, G. Milliron, N. Yaraghi, S. Herrera, K. Evans-Lutterodt, S.R. Nutt, P. Zavattieri, D. Kisailus, Bio-inspired impact-resistant composites, Acta Biomaterialia 10 (2014) 3997–4008, doi:10.1016/j.actbio.2014.03.022.

[2] P.Y. Chen, A.G. Stokes, J. McKittrick, Comparison of the structure and mechanical properties of bovine femur bone and antler of the North American elk (Cervus elaphus canadensis), Acta Biomaterialia 5 (2) (2009) 693–706, doi:10.1016/j.actbio.2008.09.011.

[3] M. Viani, T. E. Scha, J. B. Thompson, N. A. Frederick, J. Kindt, and P. K. Hansma, "Molecular mechanistic origin of the toughness of natural adhesives, ® bres and composites," vol. 399, no. June, pp. 761–763, 1999.

[4] A. Lin, M.A. Meyers, Growth and structure in abalone shell, Materials Science & Engineering A 390 (2005) 27–41, doi:10.1016/j.msea.2004.06.072.

[5] M.I. Lopez, P.E. Meza, M.A. Meyers, Organic interlamellar layers, mesolayers and mineral nanobridges : Contribution to strength in abalone (Haliotis rufescence) nacre, Acta Biomaterialia 10 (5) (2014) 2056–2064, doi:10.1016/j.actbio.2013.12.016.

[6] S.E. Naleway, M.M. Porter, J. Mckittrick, M.A. Meyers, Structural Design Elements in Biological Materials : Application to Bioinspiration, Advanced Materials • 27 (37) (2015) 5455–5476, doi:10.1002/adma.201502403.

[7] U.G.K. Wegst, H. Bai, E. Saiz, A.P. Tomsia, R.O. Ritchie, Bioinspired structural materials, Nature Materials 14 (1) (2015) 23–36, doi:10.1038/nmat4089.
[8] K.J. Niklas, Plant biomechanics: An engineering approach to plant form and function 8 (3) (1993).
[9] S. Vogel, Twist-to-bend ratios and cross-sectional shapes of petioles and stems, Journal of Experimental Botany 43 (11) (1992) 1527–1532, doi:10.1093/jxb/43.11.1527.
[10] L.J. Gibson, M.F. Ashby, Cellular Solids: Structure & Properties, 2nd edition, Cambridge University Press, Cambridge, 1999.
[11] S. Skatter, B. Kucera, Tree breakage from torsional wind loading due to crown asymmetry, Forest Ecology and Management 135 (1–3) (2000) 97–103, doi:10.1016/S0378-1127(00)00301-7.
[12] S. Skatter, B. Kucera, Spiral grain - An adaptation of trees to withstand stem breakage caused by wind-induced torsion, Holz Als Roh-Und Werkstoff 55 (4) (1997) 207–213, doi:10.1007/BF02990549.
[13] G. Bazzigher, P. Schmid, Sturmschäden und Fäule, Olten, Switzerland (1969).
[14] L. Eklund, H. Säll, The influence of wind on spiral grain formation in conifer trees, Trees - Structure and Function 14 (6) (2000) 324–328, doi:10.1007/s004680050225.
[15] K.R. James, N. Haritos, P.K. Ades, Mechanical stability of trees under dynamic loads, American Journal of Botany 93 (10) (2006) 1522–1530, doi:10.3732/ajb.93.10.1522.
[16] P. Fratzl, R. Weinkamer, Nature's hierarchical materials, Progress in Materials Science 52 (8) (2007) 1263–1334, doi:10.1016/j.pmatsci.2007.06.001.
[17] S. Askarinejad, P. Kotowski, F. Shalchy, N. Rahbar, Effects of humidity on shear behavior of bamboo, Theoretical and Applied Mechanics Letters 5 (6) (2015) 236–243, doi:10.1016/j.taml.2015.11.007.
[18] P.G. Dixon, L.J. Gibson, The structure and mechanics of Moso bamboo material, Journal of The Royal Society Interface 11 (99) (2014) 1–12, doi:10.1098/rsif.2014.0321.
[19] J.F. Scherer, R.P. Bom, Determination of shear modulus in bamboo fibers composite in torsion tests, Materials Research Express 6 (3) (2019), doi:10.1088/2053-1591/aaf67e.
[20] D.W. Green, J.E. Winandy, D.E. Kretschmann, Chapter 4. Mechanical properties of wood fiber, Wood Handbook: Wood as an Engineering Material, United States Department of Agriculture, Madison, WI, 1999, pp. 1–45.
[21] S. Vogel, Twist-to-bend ratios of woody structures, Journal of Experimental Botany 46 (8) (1995) 981–985, doi:10.1093/jxb/46.8.981.
[22] E.G. Bobich, P.S. Nobel, Vegetative reproduction as related to biomechanics, morphology and anatomy of four cholla cactus species in the Sonoran Desert, Annals of Botany 87 (4) (2001) 485–493, doi:10.1006/anbo.2000.1360.
[23] A. Gibson, P.S. Nobel, The Cactus Primer, Harvard University Press, Cambridge, MA, 1986.
[24] I. Burgert, J.W.C. Dunlop, Micromechanics of Cell Walls, Mechanical Integration of Plant Cells and Plants, Springer-Verlag Berlin Heidelberg, Berlin, 2011, pp. 27–52.
[25] L. Burhenne, J. Messmer, T. Aicher, M.P. Laborie, The effect of the biomass components lignin, cellulose and hemicellulose on TGA and fixed bed pyrolysis, Journal of Analytical and Applied Pyrolysis 101 (2013) 177–184, doi:10.1016/j.jaap.2013.01.012.
[26] A.C. Wiedenhoeft, Chapter 3. Structure and Function of Wood Contents, United States Department of Agriculture, Madison, WI, 2010.
[27] D.R. Fowler, P. Prusinkiewicz, J. Battjes, D.R. Fowler, A Collision-based Model of Spiral Phyllotaxis, ACM SIGGRAPH 26 (2) (1992) 361–368.
[28] "Yearly Wind Summary (mph) Thousand Palms, California," *Desert Weather*, 2019. https://desertweather.com/windsummary.php.
[29] T. Luhmann, S. Robson, S. Kyle, J. Boehm, Close-range photogrammetry and 3D imaging, 2nd ed, Walter de Gruyter GmbH, Berlin, Germany, 2013.
[30] M.M. Porter, L. Meraz, A. Calderon, H. Choi, A. Chouhan, L. Wang, M.A. Meyers, J. McKittrick, Torsional properties of helix-reinforced composites fabricated by magnetic freeze casting, Composite Structures 119 (2015) 174–184, doi:10.1016/j.compstruct.2014.08.033.
[31] S. Amada, T. Munekata, Y. Nagase, Y. Ichikawa, A. Kirigai, Y. Zhifei, The Mechanical Structures of Bamboo in Viewpoint of Functionally Gradient and Composite Materials, Journal of Composite Materials 30 (7) (1996) 800–819.
[32] S.J. Fatihhi, A.A.R. Rabiatul, M.N. Harun, M.R.A. Kadir, T. Kamarul, A. Syahrom, Effect of torsional loading on compressive fatigue behaviour of trabecular bone, Journal of the Mechanical Behavior of Biomedical Materials 54 (2016) 21–32, doi:10.1016/j.jmbbm.2015.09.006.
[33] M. Wiemann, G. Williamson, Extreme radial changes in wood specific gravity in some tropical pioneers, Wood and fiber science 20 (3) (1988) 344–349.
[34] E.A. Wheeler, P. Baas, P.E. Gasson, IAWA LIST OF MICROSCOPIC FEATURES FOR HARDWOOD IDENTIFICATION with an Appendix on non-anatomical information IAWA Committee, IAWA Bulletin n . s 10 (3) (1989) 219–332.
[35] K. Bruyere Garnier, R. Dumas, C. Rumelhart, and M. E. Arlot, "Mechanical characterization in shear of human femoral cancellous bone: torsion and shear tests'," vol. 21, no. 1999, pp. 641–649, 2000.
[36] C.C. Gerhards, Effect of Moisture Content and Temperature on the Mechanical Properties of Wood: An Analysis of Immediate Effects, Wood and Fiber 14 (1) (1982) 4–36 [Online]. Available: http://wfs.swst.org/index.php/wfs/article/viewFile/501/501 .
[37] J.W.C. Dunlop, R. Weinkamer, P. Fratzl, Artful interfaces within biological materials, Materials Today 14 (3) (2011) 70–78, doi:10.1016/S1369-7021(11)70056-6.
[38] F. Barthelat, Z. Yin, M. Buehler, Structure and mechanics of interfaces in biological materials, Nature Reviews Materials 1 (2016) 1–16.
[39] O. Speck, M. Schlechtendahl, F. Schmich, T. Speck, Self-Healing Processes in Plants – a Treasure Trove for Biomimetic Self-Repairing Materials, ICSHM 2013: Proceedings of the 4th International Conference on Self-Healing Materials 2 (2013) 53–56.
[40] O. Speck, T. Speck, An Overview of Bioinspired and Biomimetic Self-Repairing Materials, Biomimetics 4 (1) (2019) 26, doi:10.3390/biomimetics4010026.
[41] P.K. Mallick, Fiber-Reinforced Composites, 3rd ed, Taylor & Francis Group, Boca Raton, FL, 2008.
[42] T. Masselter, S. Eckert, and T. Speck, "Functional morphology, biomechanics and biomimetic potential of stem – branch connections in Dracaena reflexa and Freycinetia insignis," no. 173, pp. 173–185, 2011, doi: 10.3762/bjnano.2.21.
[43] D. Trupiano, A. Di, A. Montagnoli, and B. Lasserre, "Involvement of lignin and hormones in the response of woody poplar taproots to mechanical stress," pp. 39–52, 2012, doi: 10.1111/j.1399-3054.2012.01601.x.
[44] D. Chiatante, M. Sarnataro, S. Fusco, A. Di Iorio, G. S. Scippa, M. Sarnataro, S. Fusco, A. Di Iorio, and G. S. Scippa, "Modification of root morphological parameters and root architecture in seedlings of Fraxinus ornus L . and Spartium junceum L . growing on slopes Modification of root morphological parameters and root architecture in seedlings of Fraxinus ornus L . and Sp," vol. 3504, 2006, doi: 10.1080/11263500312331351321.
[45] D. Chiatante, M. Beltotto, E. Onelli, A. Di Iorio, A. Montagnoli, S. G. Scippa, M. Beltotto, E. Onelli, A. Di Iorio, A. Montagnoli, and S. G. Scippa, "New branch roots produced by vascular cambium derivatives in woody parental roots of Populus nigra L . parental roots of Populus nigra L.," vol. 3504, 2010, doi: 10.1080/11263501003718612.
[46] F.C. Meinzer, B. Lachenbruch, T.E. Dawson, Size-and Age-Related Changes in Tree Structure and Function, Springer Dordrecht Heidelberg, Dodrecht, 2011.
[47] H. Kim, K. Kim, S.J. Lee, Hydraulic Strategy of Cactus Root–Stem Junction for Effective Water Transport, Frontiers in Plant Science 9 (June) (2018), doi:10.3389/fpls.2018.00799.
[48] J.F. Stevenson, J.D. Mauseth, Effects of Environment on Vessel Characters in Cactus Wood, International Journal of Plant Sciences 165 (3) (2004) 347–357, doi:10.1086/382807.
[49] J. D. Mauseth, "Water-storing and Cavitation-preventing Adaptations in Wood of Cacti Author (s): JAMES D . MAUSETH Source : Annals of Botany, Vol . 72, No . 1 (July 1993), pp . 81-89 Published by : Oxford University Press Stable URL : https://www.jstor.org/stable/4," vol. 72, no. 1, pp. 81–89, 2019.
[50] J. Ju, H. Bai, Y. Zheng, T. Zhao, R. Fang, L. Jiang, A multi-structural and multi-functional integrated fog collection system in cactus, Nature Communications 3 (2012) 1246–1247, doi:10.1038/ncomms2253.
[51] A. Gibson, Comparative anatomy of secondary xylem in cactoideae, Biotropica 5 (1) (1973) 29–65.
[52] J.D. Mauseth, Comparative structure-function studies within a strongly dimorphic plant, Melocactus intortus (Cactaceae), Bradleya 7 (1989) 1–12, doi:10.25223/brad.n7.1989.a1.
[53] R.M. Ogburn, E.J. Edwards, The ecological water-use strategies of succulent plants, 55, 1st ed, Elsevier Ltd, 2010.
[54] "Norway Spruce (Picea abies) 11.3 m," *CG Axis*, 2010. https://cgaxis.com/product/norway-spruce-picea-abies-11-3m/.
[55] H. Säll, Spiral Grain in Norway Spruce, Växjö University (2002).
[56] "Bamboo Anatomy and Growth Habits, " *Bamboo Botanicals*, 2019. http://www.bamboobotanicals.ca/html/about-bamboo/bamboo-growth-habits.html.
[57] E. Kanzawa, S. Aoyagi, T. Nakano, Vascular bundle shape in cross-section and relaxation properties of Moso bamboo (Phyllostachys pubescens), Materials Science and Engineering C 31 (5) (2011) 1050–1054, doi:10.1016/j.msec.2011.03.004.
[58] R. Gooding, Bamboo Photo Gallery, Peak Bamboo (2018) https://peakbamboo.com/gallery/.
[59] M. Rizzo, Staghorn Cholla Cactus Fruit, Pics4Learning (2009) https://www.pics4learning.com/details.php?img=staghornchollacactus.jpg.